Materials Today Communications 51 (2026) 114737

Contents lists available at ScienceDirect

Materials Today Communications

journal homepage: www.elsevier.com/locate/mtcomm

Mode-I and mode-II interlaminar fracture properties of high strength polyacrylonitrile-based carbon fiber reinforced disulfide-based epoxy-covalent adaptable network polymer composite

Kimiyoshi Naito [a,b,*], Yasuyuki Nakamura [c], Shota Ando [c,d], Jun Koyanagi [e], Keiichi Shirasu [f], Makoto Watanabe [a], Takaya Suzuki [g], Hiroaki Kuwahara [g]

[a] National Institute for Materials Science (NIMS), Research Center for Structural Materials, 1-2-1 Sengen, Tsukuba, Ibaraki 305-0047, Japan
[b] Tohoku University, Department of Aerospace Engineering, 6-6-01, Aoba, Aramaki, Aoba-ku, Sendai, Miyagi 980-8579, Japan
[c] National Institute for Materials Science (NIMS), Research Center for Macromolecules and Biomaterials, 1-2-1 Sengen, Tsukuba, Ibaraki 305-0047, Japan
[d] The University of Tokyo, Department of Advanced Materials Science, 5-1-5, Kashiwanoha, Kashiwa, Chiba 277-8561, Japan
[e] Tokyo University of Science, Department of Materials Science and Technology, 6-3-1 Niijuku, Katsushika-ku, Tokyo 125-8585, Japan
[f] Tohoku University, Department of Finemechanics, 6-6-01, Aoba, Aramaki, Aoba-ku, Sendai, Miyagi 980-8579, Japan
[g] Teijin Limited, Manufacture and sales of carbon fiber products, 234, Kamitogari, Nagaizumi-cho, Sunto-gun, Shizuoka 411-8720, Japan

ARTICLE INFO

Keywords:
Carbon fiber reinforced plastics
Epoxy-covalent adaptable network (CAN)
Interlaminar fracture property

ABSTRACT

Advances have focused on disulfide-based epoxy-covalent adaptable network (CAN) polymer systems, which leverage reversible disulfide exchange reactions. The evolution from conventional carbon fiber reinforced thermosetting composites (CFRPs) to disulfide-based epoxy-CAN polymer composites represents a paradigm shift toward sustainable, high-performance materials. Recently, Teijin Ltd. has developed disulfide-based epoxy-CAN CFRP (carbon fiber: IMS65; resin: DGEBA/4-APD/PES5003P (disulfide-based epoxy-CAN polymer)). In this study, the mode-I and mode-II interlaminar fracture properties of the disulfide-based epoxy-CAN CFRP were investigated. The mode-I and mode-II interlaminar fracture tests were conducted under static loading using a double cantilever beam and end notched flexure specimens. The values of the mode-I and mode-II interlaminar fracture toughness of the disulfide-based epoxy-CAN CFRP were 0.293 and 1.054 kN/m, which were higher than those of conventional epoxy CFRP. The fracture surfaces of the disulfide-based epoxy-CAN CFRP were rougher than those of conventional epoxy CFRP. These improvements are attributed to enhanced fiber bridging, plastic deformation, and the dynamic disulfide exchange mechanism, which promote energy dissipation and interfacial adhesion. Compared to conventional epoxy CFRPs, the novel composite exhibits superior delamination resistance, recyclability, and potential for self-healing.

1. Introduction

Carbon fiber reinforced thermosetting composites (CFRPs) have been widely used in the aerospace, automotive, and sports equipment industries due to their excellent mechanical strength, low density, thermal stability, and chemical resistance [1,2]. Compared to thermoplastics and traditional epoxy resins, CFRPs offer superior mechanical strength, fatigue resistance, dimensional stability, and long-term durability [3–5]. These composites generally utilize epoxy matrix, which form permanent covalent crosslinked networks upon curing [6]. The structural integrity of the material renders it intractable, meaning that it cannot be reshaped, repaired, or recycled. This characteristic presents significant environmental and economic challenges [7].

Conventional disposal methodologies, including incineration and landfilling, have been observed to result in the inefficient use of valuable carbon fibers and concomitant contributions to environmental degradation [8]. Mechanical recycling frequently yields products of low value due to fiber damage [9]. Conversely, thermo-chemical methods, though more effective, are energy-intensive and may degrade fiber properties [10].

To address these limitations, the concept of covalent adaptable network (CAN) polymers emerged, enabling dynamic bond exchange

---

* Corresponding author at: National Institute for Materials Science (NIMS), Research Center for Structural Materials, 1-2-1 Sengen, Tsukuba, Ibaraki 305-0047, Japan.

E-mail address: NAITO.Kimiyoshi@nims.go.jp (K. Naito).

https://doi.org/10.1016/j.mtcomm.2026.114737
Received 15 December 2025; Received in revised form 18 January 2026; Accepted 26 January 2026

reactions within thermoset matrices [11], including vitrimers introduced by Leibler et al. in 2011 [12,13] as a representative class. These polymers undergo network rearrangement and material melt through bond exchanging, imparting reprocessability, self-healing, and recyclability. Consequently, they have gained significant attention as new polymer materials class that bridge the gap between thermosets and thermoplastics [14].

Compared to traditional epoxy resins, disulfide-based epoxy-CAN polymers offer improved recyclability, reprocessability, and self-healing capabilities due to their dynamic covalent bond exchange. While traditional epoxies form permanent networks, disulfide-based systems allow for network rearrangement under thermal stimuli, enabling closed-loop material lifecycles. Advances have focused on disulfide-based epoxy-CAN polymer systems, which leverage reversible disulfide exchange reactions [15]. These systems offer several advantages: rapid stress relaxation, efficient degradation, and robust mechanical performance due to the aromatic disulfide structure [15]. For instance, Zhang et al. developed a disulfide-based epoxy-CAN polymer composite using glycerol triglycidyl ether and 4,4′-diaminodiphenyl disulfide, achieving stress relaxation within 14 s at 180 °C and complete resin degradation in 5 h [16]. This enabled effective recovery of carbon fibers with minimal loss in mechanical integrity. Moreover, these disulfide-based epoxy-CAN polymer composites demonstrate shape memory behavior, self-healing capabilities, and closed-loop recyclability, making them ideal candidates for sustainable high-performance applications [14,17]. The integration of carbon fibers into disulfide-based epoxy-CAN polymer matrices not only enhances mechanical properties but also introduces multifunctionality, such as electrical conductivity and thermal responsiveness [18]. The evolution from conventional CFRPs to disulfide-based epoxy-CAN polymer composites represents a paradigm shift toward sustainable, high-performance materials. These innovations address critical challenges in composite recycling and repair, paving the way for circular material economies in advanced engineering sectors.

Recently, Teijin Ltd. have developed carbon fiber reinforced disulfide-based epoxy-CAN polymer composites, demonstrating significant potential for sustainable material solutions. These composites exhibit enhanced recyclability and self-healing capabilities, making them suitable for next-generation structural applications. However, despite their promising features, the interlaminar fracture toughness—a critical parameter for evaluating delamination resistance and structural reliability—has not been sufficiently characterized. This study focuses on interlaminar fracture toughness because delamination is a critical failure mode in laminated composites. Understanding and improving this property is essential for ensuring structural reliability in high-performance applications.

Interlaminar fracture toughness has been shown to play a significant role in the damage propagation of CFRPs. As a result, a considerable body of research has been dedicated to developing methods for estimating it for mode-I [19,20], mode-II [20,21], and mixed modes [22]. Furthermore, previous attempts to enhance the interlaminar fracture toughness of CFRP laminates have resulted in a variety of useful outcomes. Previous studies on epoxy-dicarboxylic acid vitrimer composites have shown that interlaminar fracture toughness can be significantly improved compared to conventional epoxy systems [23]. For instance, mode I fracture energies of vitrimer laminates were found to be up to twice as high as those of standard epoxy laminates, indicating superior interfacial adhesion and damage tolerance [24].

Nevertheless, the specific interlaminar fracture behavior of Teijin's disulfide-based epoxy-CAN polymer composites remains unexplored. Understanding this property is essential for validating their applicability in demanding structural environments and for guiding future material design and optimization.

In the present work, the mode-I and mode-II interlaminar fracture properties of carbon fiber reinforced disulfide-based epoxy-CAN polymer composites developed by Teijin Ltd. were investigated. Through systematic mechanical testing and fracture surface analysis, this research seeks to elucidate the delamination resistance of these novel materials and contribute to the broader development of recyclable and high-performance composite systems. This study is the first to systematically investigate the interlaminar fracture toughness of CFRPs reinforced with disulfide-based epoxy-CAN polymers, which are emerging as promising candidates for recyclable and self-healing structural composites.

2. Experimental procedure

2.1. Materials

The CFRP laminate was produced using a unidirectional CFRP pre-impregnated material (prepreg) consisting of IMS65 (24 K) as the high strength (tensile strength of 6 GPa, tensile modulus of 290 GPa) polyacrylonitrile (PAN)-based carbon fiber (Teijin Ltd., Tokyo, Japan,) and bisphenol A diglycidyl ether (DGEBA: jER828, Mitsubishi Chemical Corp., Tokyo, Japan)/4-aminophenyl disulfide (4-APD, Merck KGaA (Sigma-Aldrich), Tokyo, Japan)-based epoxy-CAN polymer as the resin, described as SDC1–09. The disulfide-based epoxy-CAN resin used in the prepreg was subjected to the same curing cycle (180 °C for 2 h) as the composite laminate to ensure consistent thermal history and comparability. The dynamic bond exchange reaction within this disulfide-based epoxy-CAN is shown in Fig. 1(a). In the DGEBA/4-APD epoxy-CAN polymer system, the dynamic exchange is primarily driven by disulfide bond metathesis, which enables the rearrangement of the crosslinked network under thermal stimuli [25]. A hydroxyl (OH)-terminated polyether sulfone (PES5003P, Sumitomo Chemical Co. Ltd., Tokyo, Japan) was used as the toughener. The mixing ratio is 54.8: 17.9: 27.4 (DGEBA: 4-APD: PES5003P) by weight. The CFRP prepreg, supplied by Teijin Ltd., Tokyo, Japan, had a nominal thickness of 0.185 mm, a fiber areal weight of 190 g/m^2, and a resin content of 35 %; all the sheets were manufactured via conventional prepreg technology.

The CFRP laminate was also produced using a conventional epoxy unidirectional CFRP prepreg, supplied by Teijin Ltd., Tokyo, Japan, consisting of IMS65 carbon fiber and Q-11NB 130 °C-cured type epoxy as a comparison.

2.2. Specimen preparation

Fig. 1(b) shows the schematic representation of CFRP specimen preparation procedure. The CFRP prepreg sheets were trimmed to the requisite dimensions and fiber orientation. The sheets were then placed on a vacuum molding board. CFRP laminates were fabricated through the hand lay-up, with caul plate, and vacuum bagging technique (non-bleeder). The fiber and layer orientation of the composites was set to $[0]_{16}$, and the fiber volume fraction was 57.6 vol%. This value is within the typical range (55–65 %) for aerospace-grade unidirectional CFRPs [3]. The curing conditions (180 °C, 2 h, 0.49 MPa) were selected based on the prepreg manufacturer's recommendations and prior optimization studies to ensure complete crosslinking and optimal mechanical performance. The prepreg sheets were pressed at 0.490 MPa and cured at 180 °C for 2 h with a heating rate of 2 °C/min, a cooling rate of 2.5 °C/min (Q-11NB: 0.4 MPa, 130 °C for 2 h) in an autoclave (ACA Series, Ashida Mfg. Co., Ltd., Nara, Japan). The initial crack observed in the middle plane of these CFRP laminates was formed during the stacking process by the insertion of an ethylene tetrafluoroethylene release film (thickness of 25 μm; A4000R Red Release Film, Airtech International, Inc., Huntington Beach, United State).

2.3. Interlaminar fracture testing

The orientation of the fiber axis was aligned in accordance with the longitudinal direction of the test specimens, thereby defining a 0° direction for the specimen. All tests were conducted in a controlled

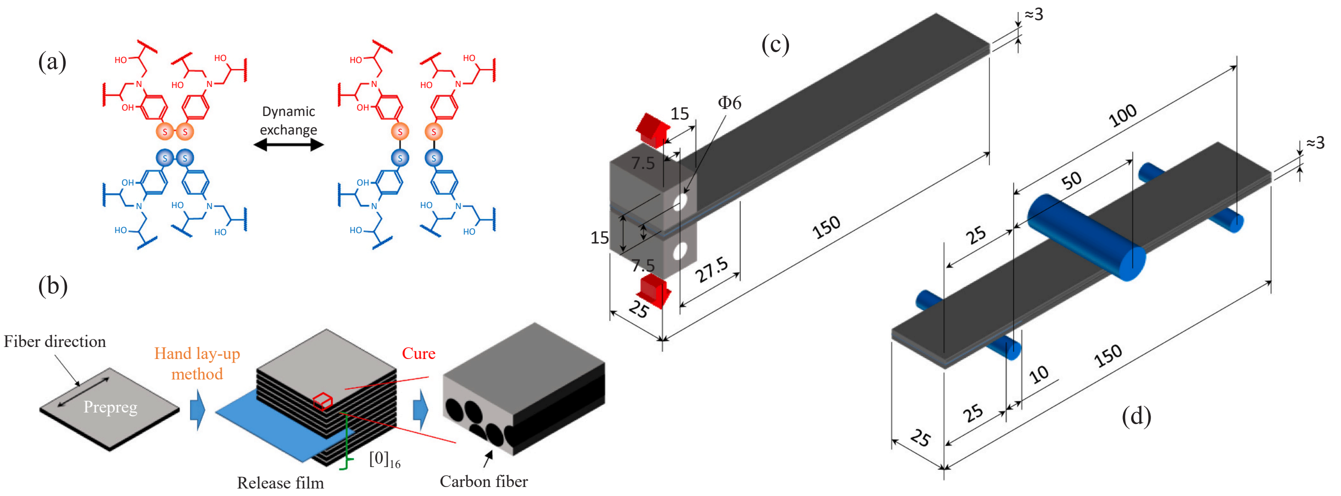

Fig. 1. Materials and specimens. (a) Dynamic bond exchange reaction within this disulfide-based epoxy-CAN polymer, (b) Schematic representation of CFRP specimen preparation procedure, (c) Double cantilever beam (DCB), and (d) End-notch flexure (ENF) specimens.

laboratory environment, with temperature maintained at 23 ± 3 °C and relative humidity set at 50 ± 5 %.

2.3.1. Mode-I interlaminar fracture property

To test the mode-I interlaminar fracture properties, double cantilever beam (DCB) specimen was used [26,27], as shown in Fig. 1(c); this had a length of 150 mm (initial delamination crack length (a_0) of 27.5 mm), a width of 25 mm, and a thickness of ~3 mm. The experimental procedure was executed by employing a table-top universal testing machine (EZ-LS, Shimadzu Corporation, Kyoto, Japan) equipped with a load cell capacity of 5 kN. The specimen was placed into the testing machine by means of a tensile jig. Prior to conducting the test, the pin that connected them was pulled upward at a rate of 1 mm/min to create a naturally shaped crack from the artificial pre-crack. The delamination crack length was measured using a digital microscope (VHX-5000 and VH-ZST, Keyence Corporation, Osaka, Japan). Subsequently, the load was removed at a rate of 1 mm/min. The tensile jig was pulled upward at a rate of 1 mm/min to estimate the compliance until a stable crack formed. At that point, the crosshead was halted and held for a period of 2 min. As the crosshead was maintained in a fixed position, the crack exhibited a gradual progression. Concurrently, the observed load underwent a slight reduction, attaining the arrest load. The occurrence of this time-dependent behavior was attributed to the formation of a stable crack front, a phenomenon that served to mitigate the impact of resin local plasticity and fiber bridging. This phenomenon was observed in both specimens. Subsequent to the initial delamination crack length measurement, the load was removed at a rate of 1 mm/min. Similar loading/unloading cycles [20] were repeated until the delamination crack length was reached more than 90 mm. Three specimens of each CFRP type prepared were tested.

The fracture surfaces were observed with a high-resolution digital microscope (VHX-8000 and VHX-7100, Keyence Corporation, Osaka, Japan) and a high-resolution scanning electron microscopy (SEM) device (Quanta 200FEG, Thermo Fisher Scientific K.K., Tokyo, Japan) at an operating voltage of 5 kV.

2.3.2. Mode-II interlaminar fracture property

To assess the mode-II interlaminar fracture properties, an end-notch flexure (ENF) specimen was utilized [27,28], as depicted in Fig. 1(d). This specimen possessed dimensions of 150 mm in length, with an a_0 value of 10 mm, a width of 25 mm, and a thickness of approximately 3 mm. The test was conducted under three-point bending conditions, with a span length of 100 mm. The apparatus utilized an XY stage, supports with a radius of curvature of 3 mm, and a table-top universal testing machine (Autograph, Shimadzu Corporation, Kyoto, Japan) with a load cell capacity of 5 kN. The specimens were then positioned on the supports, after which a load (with a radius of curvature of 6 mm) was applied quasi-statically at a crosshead speed of 0.5 mm/min. Three specimens of each CFRP type were prepared for testing.

The fracture surfaces were observed with a high-resolution digital microscope (VHX-8000 and VHX-7100, Keyence Corporation) and a high-resolution scanning electron microscopy (SEM) device (Quanta 200FEG, Thermo Fisher Scientific K.K., Tokyo, Japan) at an operating voltage of 5 kV.

Mode-I fracture testing (DCB) evaluates crack propagation under tensile opening (peel) mode, simulating delamination due to out-of-plane tensile stresses. In contrast, mode-II testing (ENF) assesses shear-driven crack propagation, representing in-plane sliding delamination. These complementary tests provide a comprehensive understanding of interlaminar toughness.

3. Results

3.1. Interlaminar fracture properties

3.1.1. Mode-I interlaminar fracture properties

Fig. 2(a) shows the load (P)–displacement (U) curves of the SDC1–09 disulfide-based epoxy-CAN polymer and Q-11NB conventional epoxy CFRP DCB specimens. Representative curves from one of the three tested specimens are shown for each material. For each loading/unloading cycle, the load exhibited a near-linear relationship with the displacement at the onset of loading, characterized as the linear deformation region. However, the absolute values of the load varied among cycles. A transition from linear to nonlinear deformation was observed as the applied load increased, coinciding with the initiation of the crack. The load reached its maximum at this point. Subsequently, the load decreased gradually, resulting in an increased displacement as the crack further propagated during the loading stage. When the crosshead was held, the crack gradually grew and the observed load slightly decreased and reached the arrest load, P_{arr}. Finally, the load exhibited a linear relationship with the displacement, indicating that the crack did not propagate during the unloading stage. The compliance ($C_I = dU/dP$) was calculated, and the delamination crack length (a) was recorded. The crack grew with an established zone of small (Q-11NB) and large (SDC1–09)-scale fiber bridging. Load in SDC1–09 was higher than that in Q-11NB. However, stick-slip behavior in SDC1–09 was lower than that in Q-11NB. It was thought to be the effects of the fiber bridging and toughener on crack growth behavior.

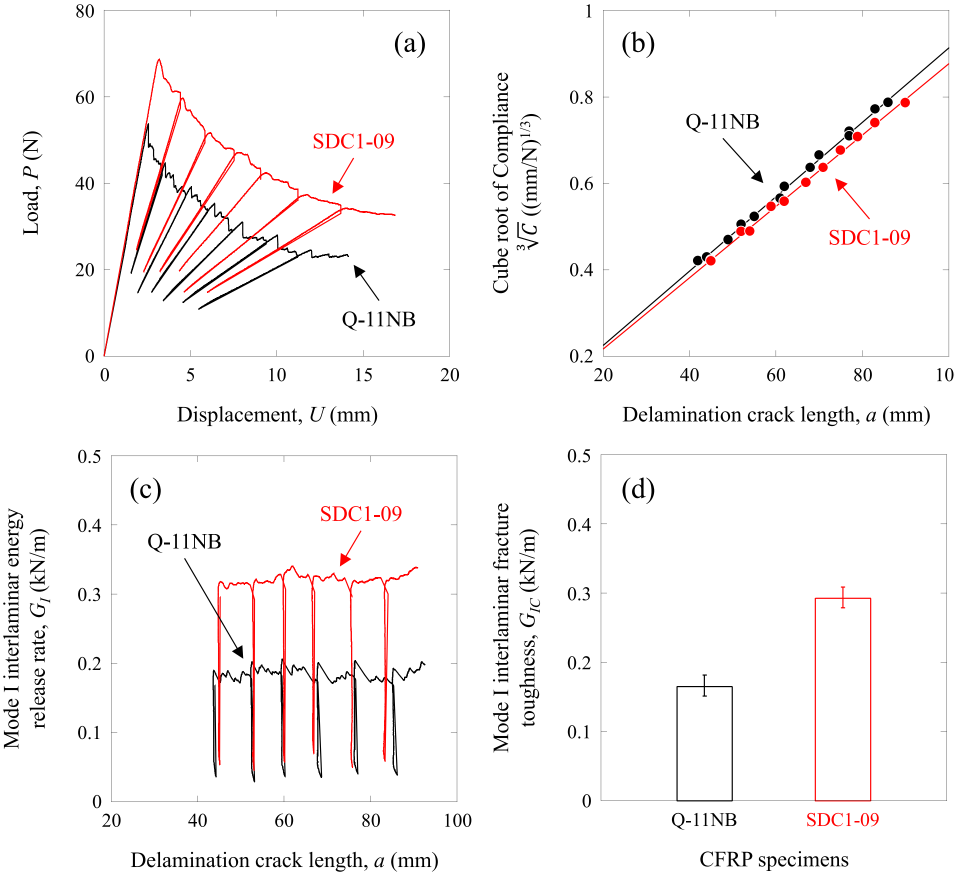

Fig. 2. Mode-I interlaminar fracture properties of the SDC1–09 disulfide-based epoxy-CAN polymer and Q-11NB conventional epoxy CFRP DCB specimens. (a)(c) Representative curves from one of the three tested specimens are shown for each material. (a) Typical load–displacement curves, (b) Relationship between cube root of compliance and delamination crack length, (c) Relationship between mode-I interlaminar energy release rate and delamination crack length (*R*-curve), and (d) Histograms of corresponding calculated mode-I interlaminar fracture toughness.

Fig. 2(b) illustrates the relationship between cube root of compliance and a of the SDC1–09 and Q-11NB CFRP DCB specimens. The energy release rate for mode-I interlaminar deformation of the DCB specimens was derived from the established relationship between compliance and a [26,27]. The deformation of the DCB specimens was thus modeled as a cantilever beam with the same length as the crack. The compliance, which encompasses local deformations such as deflection and rotation in proximity to the crack tip, was delineated as follows [29]:

$$\sqrt[3]{C_I} = \frac{2}{\sqrt[3]{EBH}}a + \frac{2}{\sqrt[3]{EB}}\chi, \tag{1}$$

where B, E, and H are the width, elastic modulus, and thickness of the adherends of the DCB specimens, respectively, and χ is a constant, whose value is 0.56 for isotropic materials [30].

The relationship between cube root of compliance and a was linear for all the DCB specimens, as follows:

$$\sqrt[3]{C_I} = A_1 a + A_2, \tag{2}$$

where A_1 and A_2 are experimental constants, obtained separately for each DCB specimen, through a least-squares fitting procedure. Subsequently, the mode-I interlaminar energy release rate (G_I) was determined by referencing the experimental A_1 and A_2 values.

The average A_1 and A_2 values were 0.00859 and 0.0537 (Q-11NB) and 0.00825 and 0.0521 (SDC1–09), respectively. The average tensile modulus, E were 137.6 and 163.7 GPa as obtained from tensile test. The average width, B and thickness of adherends, H were 25 mm and 1.5 mm, respectively. Using Eq (1), A_1 and A_2 were estimated to be 0.00859 and 0.00746 (Q-11NB), and 0.00825 and 0.00704 (SDC1–09) when the χ was 0.56. The estimated A_1 was consistent with the experimental value, while the estimated A_2 exhibited a discrepancy from the experimental value. This phenomenon appears to be attributable to the impact of anisotropy on χ. As indicated by the equations proposed by Williams [30], χ is predominantly influenced by the ratio of tensile modulus, E, and shear modulus, G. When the estimated A_2 was fitted to the experimental result, it was determined that χ and G were 2.25 (Q-11NB) and 2.53 GPa (SDC1–09), respectively. It has been determined that the predicted shear modulus is within an order of magnitude of that of unidirectional CFRPs.

The compliance calibration for DCB specimens initially used the isotropic correction factor ($\chi = 0.56$). However, discrepancies in the A_2 parameter suggested anisotropic effects. We empirically adjusted χ based on the experimental data, and the derived shear modulus values were consistent with typical unidirectional CFRP properties, as predicted by Williams' model.

The relationship between compliance and a was articulated by the following cubic formula:

$$C_I = {A_1}^3a^3 + 3{A_1}^2A_2a^2 + 3A_1{A_2}^2a + {A_2}^3 \tag{3}$$

The mode-I interlaminar energy release rate (G_I) of the CFRP specimens was calculated using the following equation:

$$G_I = \frac{P^2}{2B}\frac{dC_I}{da} = \frac{P^2}{2B}\left(3{A_1}^3a^2 + 6{A_1}^2A_2a + 3A_1{A_2}^2\right). \tag{4}$$

Fig. 2(c) displays the relationship between G_I and a (R-curve) for the SDC1–09 and Q-11NB CFRP DCB specimens. For each loading/unloading cycle, G_I was almost constant with respect to a. The slope of the R-curve for SDC1–09 was steeper than that of Q-11NB, indicating a more extensive fiber bridging zone and higher resistance to crack propagation, as shown in below discussion section. The mode-I interlaminar fracture toughness (G_{IC}) of the CFRP specimens by the arrest load, P_{arr} is defined as

$$G_{IC} = \frac{P_{arr}{}^2}{2B}\left(3A_1{}^3a^2 + 6A_1{}^2A_2a + 3A_1A_2{}^2\right) \qquad (5)$$

The G_{IC} was defined as the average G_{IC} ($G_{IC.ave}$) of the observed step of *a*.

Fig. 2(d) presents the histograms of corresponding calculated interlaminar fracture toughness, G_{IC} of the SDC1–09 and Q-11NB CFRP specimens. The SDC1–09 showed a G_{IC} of 0.293 ± 0.0095 kN/m, which was 1.7 times higher than that of Q-11NB (G_{IC} of 0.165 ± 0.0100 kN/m), demonstrating the effect of the higher fiber-bridging and toughener on the interlaminar fracture toughness [24,31].

Although only three specimens were tested per condition, the results showed consistent trends. Further testing with larger sample sizes will be conducted in future work to improve statistical significance.

3.1.2. Mode-II interlaminar fracture properties

Fig. 3(a) shows the relationship between load (*P*) and defection (δ) at the central loading point of the SDC1–09 and Q-11NB CFRP ENF specimens. Representative curves from one of the three tested specimens are shown for each material.

The load exhibited a nearly linear relationship with the deflection during the initial loading phase, which corresponded to the linear deformation region. A transition from linear to nonlinear deformation was observed as the applied load increased, coinciding with the initiation of the crack. The load subsequently reached its maximum. Subsequently, the load exhibited a precipitous decline as the crack propagated to the central loading point. The energy release rate for the mode-II interlaminar deformation of the ENF specimens was expressed as follows [27,28]:

$$G_{II} = \frac{9a_1{}^2P^2C_{II1}}{2B\left(2L^3 + 3a_1{}^3\right)}, \qquad (6)$$

where a_1 and C_{II1} denote the estimated delamination crack length and compliance at the maximum load point, respectively. The variable B corresponds to the width of the ENF specimen, while L signifies the distance from the maximum load point to the supported point. The a_1 value was calculated as [27]

$$a_1 = \left[\frac{C_{II1}}{C_{II0}}a_0{}^3 + \frac{2}{3}\left(\frac{C_{II1}}{C_{II0}} - 1\right)L^3\right]^{\frac{1}{3}}, \qquad (7)$$

where C_{II0} is defined as the initial compliance at the loading point for the linear deformation region. C_{II0} and C_{II1} represent experimental constants that are obtained separately for each ENF specimen. The mode-II interlaminar fracture toughness (G_{IIC}) of the CFRP specimens was defined as that which corresponded to the maximum G_{II}.

Fig. 3(b) illustrates the histograms of corresponding calculated interlaminar fracture toughness, G_{IIC} of the SDC1–09 and Q-11NB CFRP ENF specimens. The SDC1–09 showed a G_{IIC} of 1.054 ± 0.045 kN/m, which was 1.2 times higher than that of Q-11NB (G_{IIC} of 0.852 ± 0.065 kN/m), demonstrating the effect of the higher fiber-bridging and toughener on the interlaminar fracture toughness [31]. Although the Q-11NB specimens exhibited higher initial load values in Fig. 3(a), this is attributed to their higher initial stiffness. However, the SDC1–09 specimens demonstrated greater energy dissipation during crack propagation, resulting in higher overall fracture toughness as shown in Fig. 3(b).

Although only three specimens were tested per condition, the results showed consistent trends. Further testing with larger sample sizes will be conducted in future work to improve statistical significance.

4. Discussion

To understand the mechanisms behind the enhanced fracture toughness observed in the disulfide-based epoxy-CAN CFRP, we analyzed the interfacial bonding behavior and the molecular characteristics of the resin matrix.

Fig. 4(a) displays the relationship between G_{IC} and G_{IIC}, including the G_{IC} and G_{IIC} values in various thermoset unidirectional CFRP (IMS60 PAN-based/180 °C-cured type epoxy, T300 PAN-based/180 °C-cured type epoxy, T700SC PAN-based/130 °C-cured type epoxy, T800SC PAN-based/180 °C-cured type epoxy, M60JB PAN-based/cyanate ester, and K13C pitch-based/cyanate ester), showing that the almost former increased along with the latter [20]. However, no clear relation could be demonstrated in the G_{IC} and G_{IIC} values.

Fig. 4(b) illustrates the relationship between G_{IC}+G_{IIC} and G_{IIC}-G_{IC}, incorporating the G_{IC}+G_{IIC} and G_{IIC}-G_{IC} values in various thermoset unidirectional CFRP, demonstrating that the former increased concomitantly with the latter, thereby exhibiting an almost linear relationship [32].

The superior fracture toughness of the SDC1–09 composite can be attributed to the dynamic nature of the disulfide-based epoxy-CAN matrix. The reversible disulfide exchange reactions facilitate stress relaxation and network rearrangement under loading, which promotes localized plastic deformation around the crack tip. This behavior enhances energy dissipation during crack propagation. Furthermore, the dynamic covalent bonds improve interfacial adhesion between the

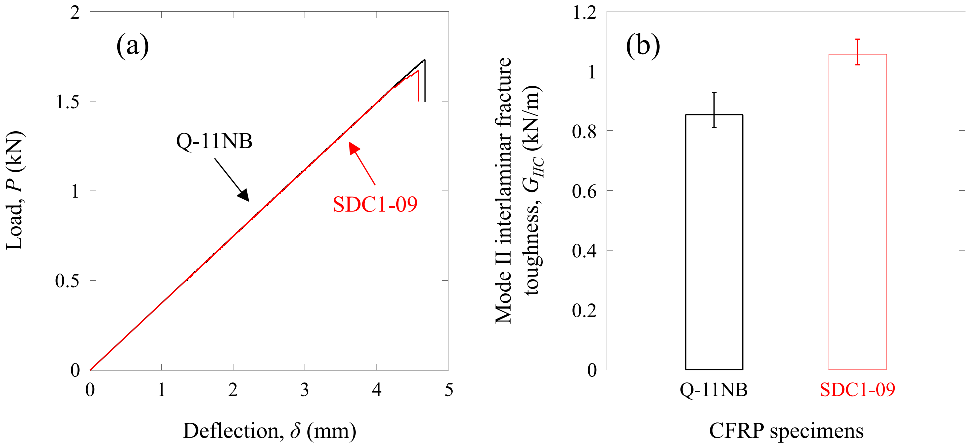

Fig. 3. Mode-II interlaminar fracture properties of the SDC1–09 and Q-11NB CFRP ENF specimens. (a) Relationship between load and defection at the central loading point. Representative curves from one of the three tested specimens are shown for each material, and (b) Histograms of corresponding calculated mode-II interlaminar fracture toughness.

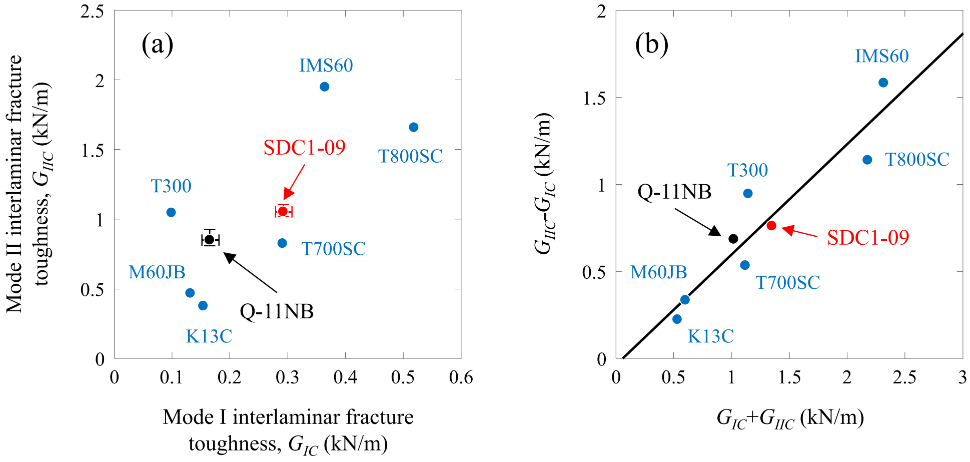

Fig. 4. (a) Relationship between mode-I and mode-II interlaminar fracture toughness, and (b) Relationship between the addition and the subtraction of mode-I and mode-II interlaminar fracture toughness.

carbon fibers and the matrix, as evidenced by the rougher fracture surfaces and extensive fiber bridging observed in SEM images. These features indicate strong interfacial bonding and a larger plastic zone, both of which contribute to improved crack resistance.

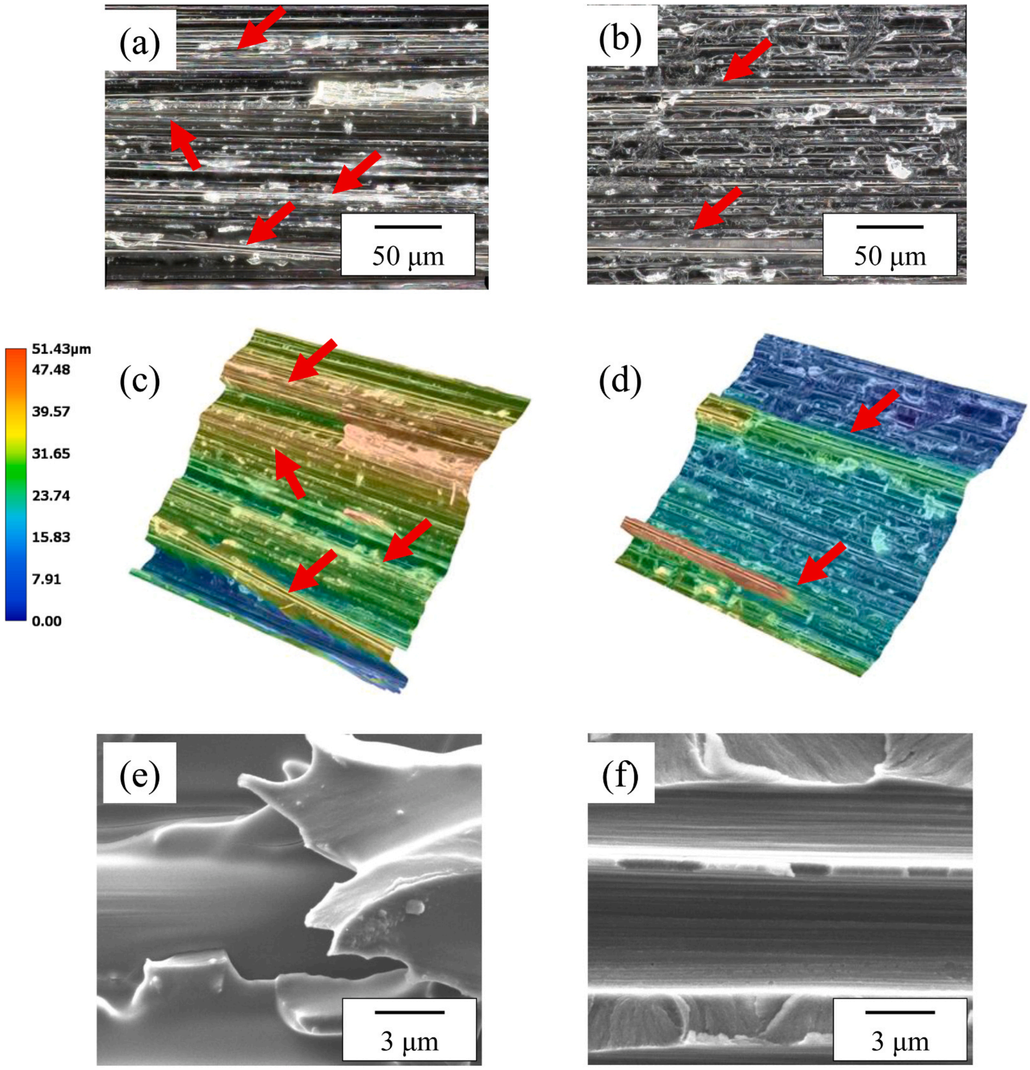

Fig. 5. Digital micrographs (DM), three-dimensional views of the corresponding to the digital micrograph images (3D-DM), and SEM micrographs (SEM) of the mode-I interlaminar fracture surfaces of the SDC1–09 and Q-11NB CFRP DCB specimens. Red arrows indicate fiber bridging at the bundle level. (a) DM, SDC1–09, (b) DM, Q-11NB, (c) 3D-DM, SDC1–09, (d) 3D-DM, Q-11NB, (e) SEM, SDC1–09, and (f) SEM, Q-11NB.

The observed relationship between G_{IC} and G_{IIC}, and linear relationship between G_{IC}+G_{IIC} and G_{IIC}-G_{IC} are likely due to the shared toughening mechanisms—namely, fiber bridging and matrix plastic deformation—which contribute similarly to both opening and shear fracture modes.

Fig. 5(a)(b) presents the digital micrographs and (c)(d) shows the three-dimensional views of the corresponding to the digital micrograph images (a)(b) of the mode-I interlaminar fracture surfaces of the SDC1–09 and Q-11NB CFRP DCB specimens. The traces of fiber bridging [33] were observed in both specimens. At the SDC1–09 specimen, larger fiber bridging was also observed, as indicated by the red arrows in Fig. 5. This larger fiber bridging is characterized by its occurrence at the bundle level.

Fig. 5(c)(d) presents the SEM micrographs of the mode-I interlaminar fracture surfaces of the SDC1–09 and Q-11NB CFRP DCB specimens. The fracture surfaces of the SDC1–09 specimens exhibited a greater degree of roughness compared to those of the Q-11NB specimens.

The fiber bridging exhibited a greater magnitude at the SDC1–09 specimen in comparison with the Q-11NB specimen (see Fig. 5(a)(b)(c)(d)). This larger fiber bridging most likely formed prior to the delamination cracking that occurred due to an early resin yielding around the crack tip [34], although the appropriate fiber bridging formed before the delamination cracking that occurred due to an early resin yielding in the Q-11NB specimen. As the plastic yield increased, microscopic damage accumulated at the wider areas on both sides of the delamination crack. When the delamination crack propagates into a large area of plastic yielding and damage previously formed ahead of it, there is an increase in fiber bridging, along with the degree of plastic deformation/damage and the size of yielding/damaged zone [35]. Consequently, the fracture surfaces exhibited a roughened texture, as illustrated in Fig. 5(e)(e). In the specimen designated Q-11NB, the delamination crack exhibited a propagation pattern that did not extend to the resin but rather to the interface between the carbon fiber and the resin, as illustrated in Fig. 5 (f). Consequently, the degree of plastic deformation/damage and the size of the yielding/damaged zone, as well as the extent of fiber bridging, were smaller than those of the SDC1–09 specimen. Consequently, the fracture surfaces exhibited a smooth appearance (see Fig. 5 (d)(f)). The mode-I fracture toughness trend exhibited a strong dependence on the degree of plastic deformation zone, as evidenced by the increasing trend in mode-I fracture toughness of the SDC1–09 DCB specimens.

Fig. 6(a)(b) presents the digital micrographs and (c)(d) shows the three-dimensional views of the corresponding to the digital micrograph images (a)(b) of the mode-II interlaminar fracture surfaces of the

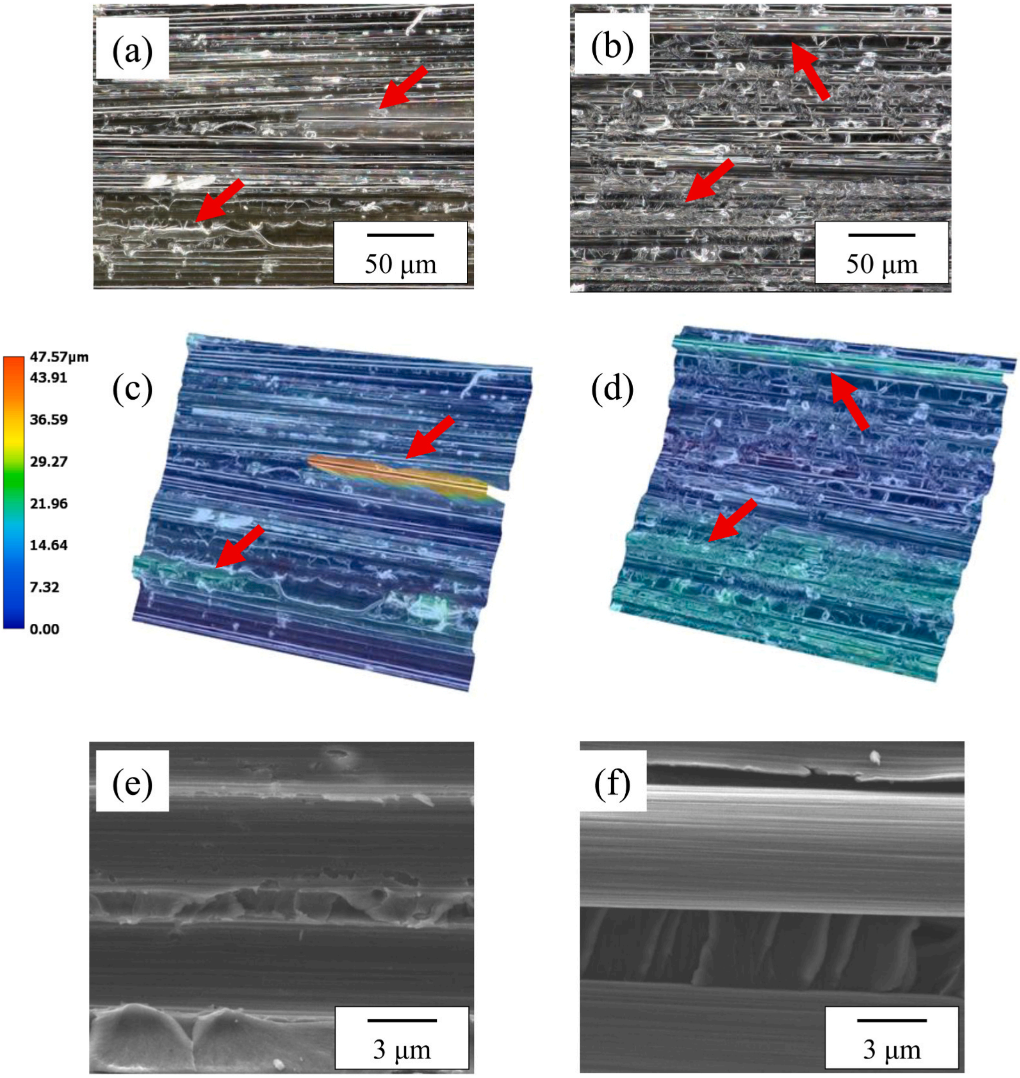

Fig. 6. Digital micrographs (DM), three-dimensional views of the corresponding to the digital micrograph images (3D-DM), and SEM micrographs (SEM) of the mode-II interlaminar fracture surfaces of the SDC1–09 and Q-11NB CFRP DCB specimens. Red arrows indicate fiber bridging at the bundle level. (a) DM, SDC1–09, (b) DM, Q-11NB, (c) 3D-DM, SDC1–09, (d) 3D-DM, Q-11NB, (e) SEM, SDC1–09, and (f) SEM, Q-11NB.

SDC1–09 and Q-11NB CFRP ENF specimens. The presence of a hackle-like fracture feature [36] was observed in both specimens, as shown in Fig. 6(e)(f). In addition, at the SDC1–09 specimen, larger fiber bridging was identified at the bundled level, as illustrated by the red arrows in Fig. 6.

As illustrated in Fig. 6(e)(f), the SEM micrographs reveal the mode-II interlaminar fracture surfaces for both SDC1–09 and Q-11NB CFRP ENF specimens. The fracture surfaces of the SDC1–09 specimens exhibited a greater degree of roughness in comparison to those of the Q-11NB specimens.

At the SDC1–09 specimen, ductile hackle pattern was observed. It is hypothesized that ductle hackle was likely formed prior to the onset of delamination cracking, a phenomenon attributed to early resin yielding around the crack tip [37]. As the plastic yield increased, microscopic damage accumulated at the broader regions on both sides of the delamination crack. This phenomenon also occurred in the DCB specimens, along with yielding and microscopic damage [38]. The mode-II fracture toughness trend exhibited a strong dependence on the degree of plastic deformation zone, as evidenced by the increasing trend in mode-II fracture toughness of the SDC1–09 ENF specimens.

Quantitative analysis of the fracture surfaces revealed that the average fiber bridging lengths in SDC1–09 were approximately 150 μm (mode-I in Fig. 5) and 100 μm (mode-II in Fig. 6), compared to 80 μm (mode-I in Fig. 5) and 50 μm (mode-II in Fig. 6) in Q-11NB. The bridging densities were also higher in SDC1–09.

The enhancing mechanisms for the mode-I and mode-II interlaminar fracture toughness were found to be analogous, and a linear relationship was observed between the two interlaminar fracture toughness types, as illustrated in Fig. 4.

The results revealed that the Teijin's disulfide-based epoxy-CAN polymer composite exhibit enhanced delamination resistance, indicating improved structural reliability. Fracture surface analysis further confirmed strong interfacial adhesion and energy dissipation mechanisms, contributing to the material's superior damage tolerance. The key innovation lies in the integration of disulfide-based epoxy-CAN polymer chemistry into CFRP systems. By leveraging reversible disulfide exchange reactions, these composites demonstrate: reprocessability and recyclability without significant degradation of fiber or matrix properties, self-healing capabilities through dynamic covalent bond rearrangement, shape memory behavior and thermal responsiveness, enhancing multi-functionality. This represents a paradigm shift from traditional, intractable thermoset composites to adaptive, sustainable materials with closed-loop lifecycle potential. The disulfide-based epoxy-CAN CFRPs are highly suitable for next-generation structural applications in: Aerospace and automotive industries, where lightweight, durable, and repairable materials are critical, sports equipment, benefiting from the material's toughness and recyclability, sustainable engineering systems, supporting circular economy goals through material reuse and reduced environmental impact. The improved interlaminar fracture toughness further validates their use in high-performance, load-bearing components where delamination resistance is essential.

Although this study focuses on fracture behavior, future work will investigate the self-healing and reprocessability features of the disulfide-based epoxy-CAN matrix to directly demonstrate its adaptive functionality.

5. Conclusions

This study presents the first comprehensive evaluation of interlaminar fracture toughness in disulfide-based epoxy-CAN CFRPs. The mode-I and mode-II interlaminar fracture properties of unidirectional, high strength PAN-based carbon fiber and disulfide-based epoxy-CAN CFRP were investigated. The results are summarized below.

1) The disulfide-based epoxy-CAN CFRP exhibited significantly higher mode-I and mode-II interlaminar fracture toughness compared to conventional epoxy CFRP.
2) The enhanced toughness is attributed to fiber bridging, plastic deformation, and dynamic disulfide bond exchange.
3) The mode-II interlaminar fracture toughness increased along with the mode-I one, and the addition of mode-I and mode-II interlaminar fracture toughness increased along with subtraction one, revealing a linear relationship between them.
4) Fracture surface analysis revealed rougher textures and larger bridging zones in the disulfide-based system.
5) These findings support the potential of disulfide-based epoxy-CAN CFRPs for sustainable, high-performance structural applications, including aerospace, automotive, and recyclable engineering systems.

CRediT authorship contribution statement

Hiroaki Kuwahara: Writing – review & editing, Validation, Supervision, Resources, Methodology, Investigation, Data curation, Conceptualization. **Takaya Suzuki:** Writing – review & editing, Validation, Supervision, Resources, Methodology, Investigation, Data curation, Conceptualization. **Makoto Watanabe:** Writing – review & editing, Validation, Supervision, Methodology, Investigation, Data curation. **Keiichi Shirasu:** Writing – review & editing, Validation, Supervision, Methodology, Investigation, Data curation. **Jun Koyanagi:** Writing – review & editing, Validation, Supervision, Methodology, Investigation, Data curation. **Shota Ando:** Writing – review & editing, Validation, Supervision, Methodology, Investigation, Data curation. **Yasuyuki Nakamura:** Writing – review & editing, Validation, Supervision, Methodology, Investigation, Data curation. **Kimiyoshi Naito:** Writing – review & editing, Writing – original draft, Visualization, Validation, Supervision, Software, Resources, Methodology, Investigation, Formal analysis, Data curation, Conceptualization.

Funding

This work was supported by JST K Program Grant Number JPMJKP24W1, Japan.

Declaration of Competing Interest

The authors declare the following financial interests/personal relationships which may be considered as potential competing interests. Kimiyoshi Naito reports financial support was provided by National Institute for Materials Science. If there are other authors, they declare that they have no known competing financial interests or personal relationships that could have appeared to influence the work reported in this paper.

Data availability

Data will be made available on request.

References

[1] J. Zhang, G. Lin, U. Vaidya, H. Wang, Past, present and future prospective of global carbon fibre composite developments and applications, Compos. B Eng. 250 (2023) 110463, https://doi.org/10.1016/j.compositesb.2022.110463.

[2] H. Wang, S. Huo, V. Chevali, W. Hall, A. Offringa, P. Song, H. Wang, Carbon fiber reinforced thermoplastics: From materials to manufacturing and applications, Adv. Mater. 37 (2025) 2418709, https://doi.org/10.1002/adma.202418709.

[3] Z. Lu, M. Jiang, Y. Pan, G. Xian, M. Yang, Durability of basalt fibers, glass fibers, and their reinforced polymer composites in artificial seawater, Polym. Compos 43 (2022) 1961–1973, https://doi.org/10.1002/pc.2651.

[4] Z. Zhang, Q. Ji, Z. Guo, C. Li, R. Guo, J. Tian, Z. Zhang, T. He, G. Xian, Design, preparation, and mechanical properties of glass fiber reinforced thermoplastic self-anchor plate cable exposed in alkaline solution environment, Polym. Compos 45 (2024) 11687–11700, https://doi.org/10.1002/pc.28591.

[5] R. Guo, G. Xian, F. Li, C. Li, B. Hong, Hygrothermal resistance of pultruded carbon, glass and carbon/glass hybrid fiber reinforced epoxy composites, Constr. Build. Mater. 315 (2022) 125710, https://doi.org/10.1016/j.conbuildmat.2021.125710.

[6] R. Yang, L. Gan, J. Huang, Enhancing heat-resistance of epoxy with conductive and crosslink networks by designing imide-based chain extender, J. Polym. Res. 31 (2024) 297, https://doi.org/10.1007/s10965-024-04118-w.

[7] M. Hamed, C. Zhang, A.M. Khan, M. Saleem, M.D. Musanu, Holistic review of drilling on CFRP composites: Techniques, FEM, sustainability, challenges, and advances, Int. J. Adv. Manuf. Technol. 135 (2024) 2661–2696, https://doi.org/10.1007/s00170-024-14317-w.

[8] M. Yuan, Z. Li, Z. Teng, Progress and prospects of recycling technology for carbon fiber reinforced polymer, Front. Mater. 11 (2024) 1484544, https://doi.org/10.3389/fmats.2024.1484544.

[9] C. Vega-Leal, C. Zárate-Pérez, V.A. Gomez-Culebro, M. Burelo, E.A. Franco-Urquiza, C.D. Treviño-Quintanilla, Mechanical recycling of carbon fibre reinforced polymers. Part 1: influence of cutting speed on recycled particles and composites properties, Int. J. Sustain. Eng. 17 (2024) 1–10, https://doi.org/10.1080/19397038.2024.2324359.

[10] N.F. Torkaman, W. Bremser, R. Wilhelm, Catalytic recycling of thermoset carbon fiber-reinforced polymers, ACS Sustain. Chem. Eng. 12 (2024) 7668–7682, https://doi.org/10.1021/acssuschemeng.3c06613.

[11] S. Kamarulzaman, Z.M. Png, E.Q. Lim, I.Z.S. Lim, Z. Li, S.S. Goh, Covalent adaptable networks from renewable resources: Crosslinked polymers for a sustainable future, Chem 9 (2023) 2771–2816, https://doi.org/10.1016/j.chempr.2023.04.024.

[12] D. Montarnal, M. Capelot, F. Tournilhac, L. Leibler, Silica-like malleable materials from permanent organic networks, Science 334 (2011) 965–968, https://doi.org/10.1126/science.1212648.

[13] M. Capelot, M.M. Unterlass, F. Tournilhac, L. Leibler, Catalytic control of the vitrimer glass transition, ACS Macro. Lett. 1 (2012) 789–792, https://doi.org/10.1021/mz300239f.

[14] A.M. Hubbard, Y. Ren, A. Sarvestani, D. Konkolewicz, C.R. Picu, A.K. Roy, V. Varshney, D. Nepal, Recyclability of vitrimer materials: Impact of catalyst and processing conditions, ACS Omega 7 (2022) 29125–29134, https://doi.org/10.1021/acsomega.2c02677.

[15] S. Begum, K. Kutonova, A. Mauri, M. Koenig, K.C. Chan, C. Sprau, C. Dolle, V. Trouillet, Z. Hassan, T. Leonhard, S. Heißler, Y.M. Eggeler, W. Wenzel, M. Kozlowska, S. Bräse, Disulfide-bridged dynamic covalent triazine polymer thin films by interface polymerization: High refractive index with excellent optical transparency, Adv. Func. Mate 34 (2024) 2303929, https://doi.org/10.1002/adfm.202303929.

[16] Q. Zhang, M. Li, P. Feng, L. Meng, X. Jian, J. Xu, Rapid stress relaxation and degradable aromatic disulfide vitrimer for recyclable carbon fiber reinforced composite, J. Polym. Res. 31 (2024) 87, https://doi.org/10.1007/s10965-024-03939-z.

[17] N. Lorenz, W.E. Dyer, B. Kumru, High-performance vitrimer entailing renewable plasticizer engineered for processability and reactivity toward composite applications, ACS Appl. Polym. Mater. 7 (2025) 1934–1946, https://doi.org/10.1021/acsapm.4c03731.

[18] J. Hong, Y. Hong, J. Jeong, D. Oh, M. Goh, Robust biobased vitrimers and its application to closed-loop recyclable carbon fiber-reinforced composites, ACS Sustain. Chem. Eng. 11 (2021) 14112–14123, https://doi.org/10.1021/acssuschemeng.3c03468.

[19] Z. Saka Dinç, Y. Öz, P. Potluri, W.W. Sampson, H.A. Eren, Influence of thermoplastic fibre-epoxy adhesion on the interlaminar fracture toughness of interleaved polymer composites, Compos. Part A Appl. Sci. Manuf. 189 (2025) 108619, https://doi.org/10.1016/j.compositesa.2024.108619.

[20] K. Naito, C. Nagai, Mode-I and mode-II interlaminar fracture properties of high modulus pitch-based carbon fiber reinforced polymers containing different nanostructures, J. Compos. Mater. 56 (2022) 397–407, https://doi.org/10.1177/00219983211049289.

[21] B. Yenigun, M.S. Chaudhry, E. Gkouti, A. Czekanski, Characterization of mode I and mode II interlaminar fracture toughness in CNT-enhanced CFRP under various temperature and loading rates, Nanomaterials 13 (2023) 1729, https://doi.org/10.3390/nano13111729.

[22] M. Arai, T. Sasaki, S. Hirota, H. Ito, N. Hu, M. Quaresimin, Mixed modes interlaminar fracture toughness of cfrp laminates toughened with CNF interlayer, Acta Mech. Solid. Sin. 25 (2012) 321–330, https://doi.org/10.1016/S0894-9166(12)60029-9.

[23] K. Tangthana-umrung, M. Gresil, Interlaminar fracture toughness behaviour of carbon fibre reinforced polymer with epoxy-dicarboxylic acid vitrimer matrix, Compos. Commun. 32 (2022) 101182, https://doi.org/10.1016/j.coco.2022.101182.

[24] H. Bai, R. Bai, T. Zhao, Z. Lei, Q. Li, C. Yan, X. Hong, C. Liu, Multiscale experimental characterisation of mode-I interfacial fracture behaviour of vitrimer composites, Mater. Des. 233 (2023) 112229, https://doi.org/10.1016/j.matdes.2023.112229.

[25] U.F. Fritze, M. Von Delius, Dynamic disulfide metathesis induced by ultrasound, Chem. Commun. 52 (2016) 6363–6366, https://doi.org/10.1039/c6cc02034h.

[26] ASTM D5528/D5528M-21, Standard test method for mode I interlaminar fracture toughness of unidirectional fiber-reinforced polymer matrix composites, West Conshohocken, ASTM International, 2021. https://doi.org/10.1520/D5528_D5528M-21.

[27] JIS K7086:1993, Testing methods for interlaminar fracture toughness of carbon fibre reinforced plastics, Tokyo, Japanese Industrial Standards Committee, 1993.

[28] ASTM D7905/D7905M-19e1, Standard test method for determination of the mode II interlaminar fracture toughness of unidirectional fiber-reinforced polymer matrix composites, West Conshohocken, ASTM International, 2019. https://doi.org/10.1520/D7905_D7905M-19E01.

[29] A. Tabiei, W. Zhang, Composite laminate delamination simulation and experiment: A review of recent development, Appl. Mech. Rev. 70 (2018) 030801, https://doi.org/10.1115/1.4040448.

[30] J.G. Williams, The fracture mechanics of delamination tests, J. Strain Anal. Eng. Des. 24 (1989) 207–214, https://doi.org/10.1243/03093247V244207.

[31] L. Adamos, R. Alderliesten, T. Loutas, A new interpretation of mode I interlaminar fracture in layered materials, Eng. Fract. Mech. 309 (2024) 110400, https://doi.org/10.1016/j.engfracmech.2024.110400.

[32] L. Chen, L.W. Wu, Q. Jiang, D. Tian, Z. Zhong, Y. Wang, H.J. Fu, Improving interlaminar fracture toughness and impact performance of carbon fiber/epoxy laminated composite by using thermoplastic fibers, Molecules 24 (2019) 3367, https://doi.org/10.3390/molecules24183367.

[33] B. Liu, S. Cao, N. Gao, L. Cheng, Y. Liu, Y. Zhang, D. Feng, Thermosetting CFRP interlaminar toughening with multi-layers graphene and MWCNTs under mode I fracture, Compos. Sci. Technol. 183 (2019) 107829, https://doi.org/10.1016/j.compscitech.2019.107829.

[34] M. Ghavami pour, S.S.R. Koloor, M. Petrů, M.R. Ayatollahi, Critical review of interlaminar damage process and failure analysis in fiber-reinforced composite laminates encompassing fiber-bridging phenomenon, J. Compos. Mater. 59 (2025) 1553–1591, https://doi.org/10.1177/00219983251313669.

[35] H. Ben Gur, L. Banks-Sills, Evaluation of the effect of fiber bridging on mode I quasi-static testing, Fatigue Fract. Eng. Mat. Struct. 46 (2023) 1357–1374, https://doi.org/10.1111/ffe.13930.

[36] R. Ufuk, K. Bilge, B.E. Kıral, M. Ereke, A. Karabeyoğlu, Fractographic investigation of cryogenic temperature mode-II delamination behavior of filament wound CFRP kaminates with varied resin systems, J. Compos. Sci. 7 (2023) 450, https://doi.org/10.3390/jcs7110450.

[37] S. Meister, J. Stüve, R.M. Groves, Optical material characterisation of prepreg CFRP for improved composite inspection, Appl. Compos. Mater. 29 (2022) 871–887, https://doi.org/10.1007/s10443-021-09994-9.

[38] W. Tu, J.A. Pascoe, R. Alderliesten, Comparison of mode II delamination behaviours in multidirectional and unidirectional composite laminates, Compos. B Eng. 291 (2025) 111941 https://doi.org/0.1016/j.compositesb.2024.111941.